

Spectroscopic Properties of $[\text{Pt}_2(\mu\text{-P}_2\text{O}_5\text{H}_2)_4]^{4-}$: A Time-Dependent Density Functional Theory and Conductor-like Polarizable Continuum Model Investigation

Stanislav R. Stoyanov, John M. Villegas, and D. Paul Rillema*

Department of Chemistry, Wichita State University, 1845 North Fairmount Street, Box 51,
Wichita, Kansas 67260-0051

Received: April 14, 2004; In Final Form: June 12, 2004

The calculation of the singlet ground-state (SGS) and the lowest-lying triplet-state (LLTS) geometries of $[\text{Pt}_2(\mu\text{-P}_2\text{O}_5\text{H}_2)_4]^{4-}$ in the gas phase using density functional theory (DFT) produces 7% Pt–Pt bond shortening in the LLTS as compared to SGS. The transition from the Pt–Pt antibonding HOMO to the bonding LUMO+1 in the gas phase and to the bonding LUMO in water creates a metal–metal σ bond in both excited states. According to the molecular orbital population analysis in water performed using the conductor-like polarizable continuum model (CPCM) and the SGS geometry, the Pt–Pt bond arises from the overlap of the metal p orbitals. The singlet excited-state energy of 27 240 cm^{-1} in the gas phase is only 40 cm^{-1} higher than the experimental absorption energy. The first triplet excited-state energy of 22 730 cm^{-1} in the gas phase and 22 810 cm^{-1} in water correlates with the experimental phosphorescence excitation energy of 22 100 cm^{-1} . The energy of the LLTS correlates with the experimental phosphorescence emission energy.

Introduction

Square-planar complexes of d^8 transition metals are known to exhibit unusual photochemical properties.¹ They differ from the octahedral and tetrahedral complexes by the presence of open axial coordination sites where binding can occur. Some square-planar complexes^{1c} of Pt(II) such as $[\text{Pt}(\text{bpy})_2]^{2+}$, where bpy is 2,2'-bipyridine, and $[\text{Pt}(\text{CN})_4]^{2-}$ utilize these sites to form crystals of axially stacked complexes. There is also strong evidence for the formation of dimers in solution where the units are held together by Pt–Pt binding amplified by ligand π – π interaction.^{1d,2}

Square-planar Pt(II) complexes have been subjected to a number of theoretical studies in the past few years.³ The results of DFT and TDDFT calculations have proven to be very successful tools for understanding the electronic behavior of these complexes. Frontier molecular orbital assignments were made on the basis of DFT-produced molecular orbital distributions, which provide insight into the atomic orbital contributions. Singlet excited-state energies calculated from the frontier molecular orbitals using the TDDFT method correlated quite well with absorption energies.

The formation of dimers in the lowest-lying triplet state (LLTS) of $[\text{Pt}(\text{bph})(\text{CO})_2]$ (bph = biphenyl dianion) due to stacking was investigated in our laboratory^{3c} in detail, and low-lying triplet excited states were linked to phosphorescence emission properties. Significant shortening of the Pt–Pt bond (4%) in the LLTS relative to the singlet ground state (SGS) was determined computationally and associated with the metal p_x bonding orbital of each platinum. The stacking orientation in the dimers was associated with ligand–ligand electrostatic interaction in the LLTS.^{3c}

The unique structure and emission properties of $[\text{Pt}_2(\mu\text{-P}_2\text{O}_5\text{H}_2)_4]^{4-}$ which contains bridging P–P bonded pyrophosphate ligands have been very attractive for study by investigators.⁴

Evidence for strong metal–metal interaction has been noted in the literature.^{4b} In the solid state, the complexes are stacked, forming linear chains of Pt–Pt bonds.⁵ A 7% shrinkage of the Pt–Pt distance in the LLTS relative to SGS was determined from the highly structured absorption and emission spectra of $\text{Ba}_2[\text{Pt}_2(\mu\text{-P}_2\text{O}_5\text{H}_2)_4]^{4-}$.^{4c} In an extended X-ray absorption fine structure (EXAFS) study, the Pt–Pt distance decreased by about 6%. Larger shrinkage (about 9.5%) of the Pt–Pt bond was reported on the basis of a time-resolved X-ray diffraction study of the triplet excited-state geometry of $(\text{TEA})_3\text{H}[\text{Pt}_2(\mu\text{-P}_2\text{O}_5\text{H}_2)_4]$ (TEA = tetraethylammonium ion) at 17 K.^{6a} The results in both the EXAFS and the X-ray reports were correlated with DFT calculated geometries.^{6b,c} The objective of the study reported here was to obtain further insight into the electronic properties of the binuclear complex $[\text{Pt}_2(\mu\text{-P}_2\text{O}_5\text{H}_2)_4]^{4-}$ based on our past success of studying analogous systems using theoretical DFT and TDDFT/CPCM calculations.^{3c,7}

The conductor-like polarizable continuum model (CPCM), which has been used to incorporate solvent effects into TDDFT calculations, has produced very good excited-state energies.^{4c,d} For example, it has led to dramatic changes in the excited-state energies and transition types for the $[\text{Pt}(\text{NH}_3)_4]^{2+}[\text{W}(\text{CN})_8]^{3-}$ donor–acceptor system.^{7c} The fact that these calculations lead to fairly accurate absorption energies outweighs the problem that they have overestimated the value of ϵ by factors of about 2.

Computational Technique

The geometry of $[\text{Pt}_2(\mu\text{-P}_2\text{O}_5\text{H}_2)_4]^{4-}$ (Figure 1) was optimized in the SGS using Becke's three-parameter hybrid functional B3LYP^{8a} with the local term of Lee, Yang, and Parr^{8b} and the nonlocal term of Vosko, Wilk, and Nassiar^{8c} and with the Gaussian '03⁹ (rev. B.03) program package. The Stuttgart–Dresden (SDD) ECP^{10a} was used for the Pt core potential, and Dunning/Huzinaga D95^{10b} was used for the P core potential. The (8s7p6d)/[6s5p3d]-GTO was applied for the valence shell

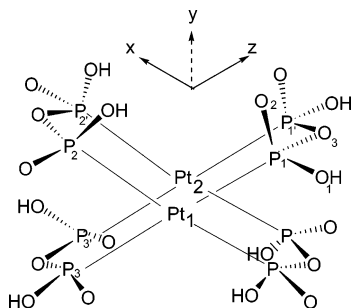
* Corresponding author. E-mail: paul.rillema@wichita.edu.

TABLE 1: Selected Geometry Parameters of $[\text{Pt}_2(\mu\text{-P}_2\text{O}_5\text{H}_2)_4]^{4-}$ Taken from X-ray Crystallography⁵ and DFT Calculated SGS and LLTS in the Gas Phase

source	Pt ₁ –Pt ₂ , Å	Pt ₁ –P ₁ , Å	P ₁ –O ₁ , Å	P ₁ –O ₂ , Å	P ₁ –P _{1'} , Å	P ₁ –O ₃ , Å	P ₁ –Pt ₁ –P ₂ , deg	P ₁ –Pt ₁ –Pt ₂ , deg
X-ray	2.925(1)	2.334(4)	1.523(14)	1.669(12)	2.970 ^a	1.629(11)	89.930 ^a	91.950 ^a
singlet	3.04	2.40	1.53	1.62	3.08	1.67	90.0	90.5
triplet	2.82	2.42	1.53	1.62	3.02	1.66	89.9	92.3

^a Standard deviations were not available.**TABLE 2: The Percent Molecular Orbital Populations of $[\text{Pt}_2(\mu\text{-P}_2\text{O}_5\text{H}_2)_4]^{4-}$ in the SGS in the Gas Phase (A) and in Aqueous Solution (B)^a**

MO	$E, \times 10^3 \text{ cm}^{-1}$	Pt									P	O	type
		s	p _x	p _y	p _z	d _{z2}	d _{xz}	d _{yz}	d _{x2-y2}	d _{xy}	$\Sigma_{s,p,d}$	$\Sigma_{s,p,d}$	
(A) In the Gas Phase													
160 (O)	35.21	0	27.4	5.2	0.2	0	0	0	2.0	1.8	26.7	36.7	O, P, Pt _{px}
161 (O)	35.22	0	0.2	0	32.3	0	0.6	3.2	0	0	26.8	36.9	O, P, Pt _{pz}
162 (O)	35.67	0	19.9	3.7	0.1	0	0	0	0.4	0.4	32.0	43.5	O, P, Pt _{px}
163 (O)	35.68	0	0.1	0	24.1	0	0.1	0.8	0	0	31.7	43.2	O, P, Pt _{pz}
164 (O)	41.62	29.4	0.7	4.2	0	12.8	0	0	18.3	20.2	8.3	6.1	Pt _s , Pt _{dx_{xy}} , Pt _{dx₂-y₂,z₂}
165 (V)	68.81	79.0	3.0	16.1	0	0.2	0	0	0.3	0.4	1.0	0	Pt _s , Pt _{py}
166 (V)	73.13	87.1	0.4	1.9	0	0	0	0	0.1	0.1	9.0	1.4	Pt _s
167 (V)	79.34	88.9	0.5	3.0	0	0.1	0	0	0.1	0.1	6.3	1.0	Pt _s
(B) In Aqueous Solution													
160 (O)	-53.51	0	19.2	3.5	6.3	0	0	0.5	1.2	1.1	28.9	39.3	O, P, Pt _{px}
161 (O)	-53.50	0	5.3	1.1	22.6	0	0.3	1.9	0.3	0.3	28.9	39.3	O, P, Pt _{pz}
162 (O)	-53.12	0	19.7	3.7	0.5	0	0	0.1	0.3	0.3	31.9	43.5	O, P, Pt _{px}
163 (O)	-53.11	0	0.5	0.1	23.4	0	0.1	0.6	0	0	31.9	43.4	O, P, Pt _{pz}
164 (O)	-44.86	26.5	0.6	3.6	0	13.7	0	0	19.6	21.7	7.6	6.7	Pt _s , Pt _{dx_{xy}} , Pt _{dx₂-y₂,d_{z2}}
165 (V)	-11.10	26.1	5.8	31.7	0	0.6	0	0	0.9	1.0	14.3	19.6	Pt _{py} , Pt _s , O, P
166 (V)	-4.80	0	0	0	0	15.5	0.6	0.1	2.5	2.7	55.7	22.9	P, O, Pt _{dz2}
167 (V)	-4.54	0	0	0	0	15.5	0.1	0	2.5	2.7	66.6	12.6	P, Pt _{i-7}

^a The orbital occupancy status is given in parentheses (O = occupied, V = virtual). The type describes the moiety with the largest share in the spatial distribution of the orbital. For example, Pt_{px} means the electron density is located on the p_x orbitals of Pt. (See text for calculation details.)**Figure 1.** Scheme of the complex ion $[\text{Pt}_2(\mu\text{-P}_2\text{O}_5\text{H}_2)_4]^{4-}$ with the coordinate system.

of Pt together with the all-electron 6-311G* basis set^{10c,d} for P, O, and H atoms of $[\text{Pt}_2(\mu\text{-P}_2\text{O}_5\text{H}_2)_4]^{4-}$.

The SGS geometry was used as a starting geometry for the LLTS geometry optimization. The geometry of the LLTS was optimized using unrestricted B3LYP and triplet multiplicity. The spin contamination from states of higher multiplicity was very low (the value of $\langle S^2 \rangle$ was 2.003).

The optimized SGS geometry in the gas phase was used for the calculation of 30 singlet excited states in the gas phase using TDDFT.¹¹ Thirty singlet excited states were also calculated in water using nonequilibrium^{12a} TDDFT and CPCM^{12,13} based on the SGS geometry in the gas phase. Several spin-forbidden triplet excited states were computed on the basis of the SGS geometry.

Results

Selected results from the geometry optimization of $[\text{Pt}_2(\mu\text{-P}_2\text{O}_5\text{H}_2)_4]^{4-}$ in the SGS and the LLTS are listed in Table 1 for comparison with the results from the X-ray crystallographic

determination of $\text{K}_4[\text{Pt}_2(\mu\text{-P}_2\text{O}_5\text{H}_2)_4] \cdot 2\text{H}_2\text{O}$.⁵ The Pt–Pt distance in the singlet ground state was 0.12 Å longer than the experimental value (2.925 Å), whereas in the triplet state it was shorter by 0.11 Å.

The atomic orbital coefficients were calculated using Mulliken population analysis. Selected atomic orbital contributions for the SGS were calculated in percent^{3c} for both the gas phase and the aqueous solution (Table 2). The sum of the percent atomic orbital contributions for Pt, P, and O atoms was 100%. The H atoms were not included. The sums of the percent orbital contributions of the s, p, and d orbitals for all eight P and all 20 O atoms were determined and tabulated. To interpret the Pt–Pt bonding in detail, the total percent contributions for the valence electrons of two Pt atoms were tabulated per s, p_x, p_y, p_z, d_{xy}, d_{xz}, d_{yz}, d_{x2-y2}, and d_{z2} orbitals. Graphical representations of selected singlet and triplet molecular orbitals in aqueous solution are shown in Figure 2. The bonding/antibonding character was determined by visual examination of the phases of the molecular orbital for each diagram. The phases are related to the spatial distributions of alpha (α) and beta (β) electron densities¹⁴ shown in red and blue colors, respectively (Figure 2).

A molecular orbital energy diagram is shown in Figure 3 for the orbitals 160–167 in the gas phase and in aqueous solution. This diagram illustrates the large difference in energies between molecular orbitals in water as compared to the gas phase. For example, the energy of the HOMO is lowered by ~87 000 cm^{−1} in water.

A number of singlet excited states were computed in the gas phase using TDDFT and in aqueous solution using TDDFT/CPCM. The singlet excited states with $f > 0.01$ are listed in Table 3. Triplet excited states were calculated in the gas phase

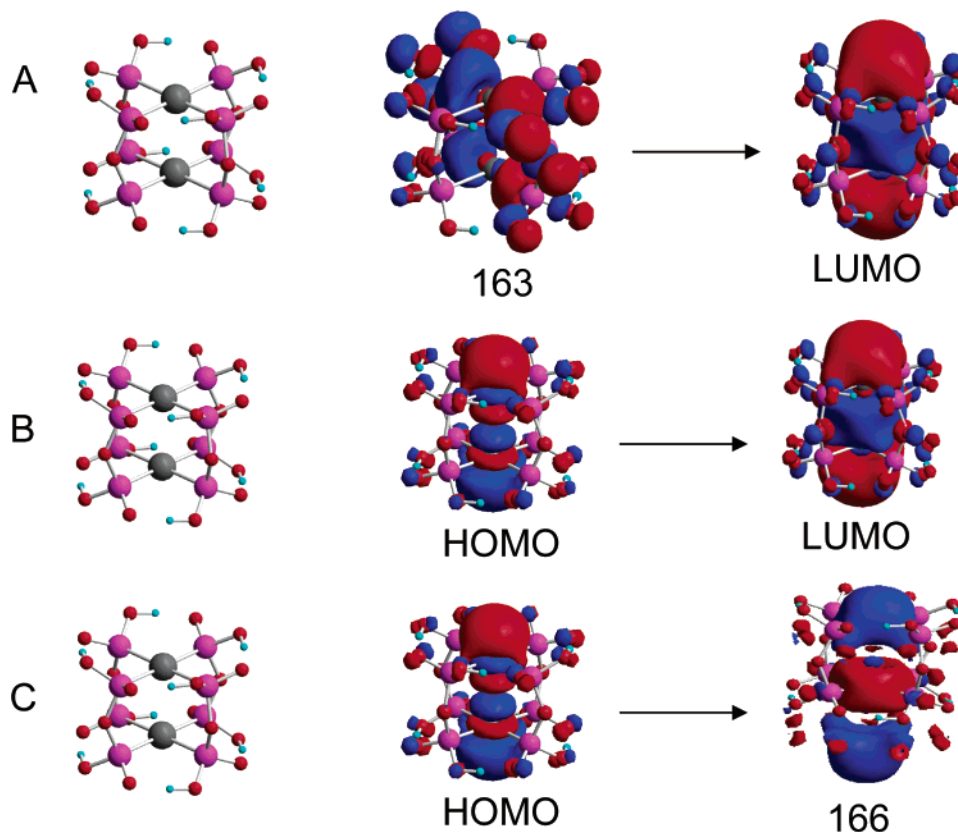


Figure 2. Graphic representations of molecular orbital transitions that were involved in the formation of selected excited states listed in Table 3. (A) Orbital 163 to LUMO (165) in water; (B) HOMO (164) to LUMO (165) in water; (C) HOMO (164) to orbital 166 in the gas phase.

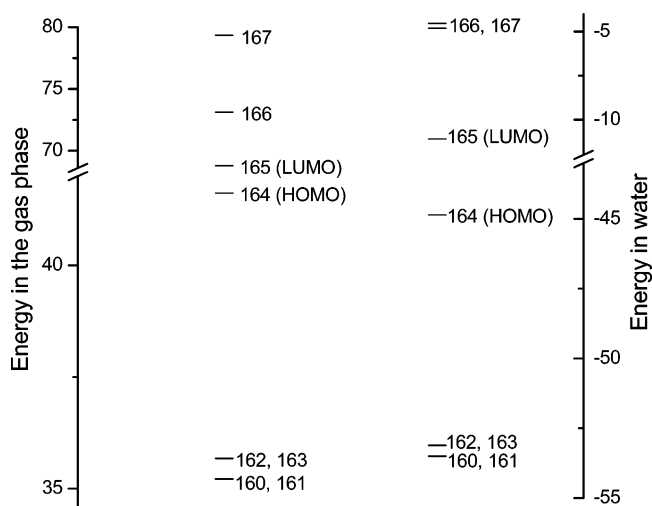


Figure 3. Molecular orbital energy ($\times 10^3 \text{ cm}^{-1}$) for orbitals 160–167 of $[\text{Pt}_2(\mu\text{-P}_2\text{O}_5\text{H}_2)_4]^{4-}$ in SGS in the gas phase and in water.

and in aqueous solution on the basis of the gas-phase SGS geometry using the above theory.

The TDDFT calculation output contained information for the excited-state energies and oscillator strengths (f). For each excited state in Table 3, the orbitals involved in the major transition are given followed by the transition coefficient in parentheses. The transition coefficients are the absolute values of the wave function coefficients for each excitation¹⁴ and are directly proportional to the contribution of the given excitation to the transition. All transitions with their transition coefficients are available as Supporting Information.

A full-width-at-half-maximum value of 1700 cm^{-1} was determined from the $27\,000 \text{ cm}^{-1}$ peak in the experimental

absorption spectrum^{4d} and was used for calculating the molar absorption coefficient (ϵ) from the oscillator strength f using eq 1.^{3c} Calculate ϵ -values are referred to below in the Discussion.

$$\epsilon = f/7.34 \times 10^{-6} \quad (1)$$

Discussion

Geometry Optimization. According to the calculations and the X-ray report,⁵ $[\text{Pt}_2(\mu\text{-P}_2\text{O}_5\text{H}_2)_4]^{4-}$ was of approximately four-fold symmetry. The SGS geometry was found to deviate slightly from it, but the LLTS geometry showed greater deviation. The fully optimized structures of both the SGS and the LLTS were of C_1 symmetry. The axes assignment in Figure 1 shows the y axis along the Pt–Pt bond, while the x and the z axes are along the Pt–P bonds. These assignments and the point group are different from those used by past investigators^{4d} who chose to use the higher symmetry for interpreting the results, recognizing that it was a simplification.

For the $[\text{Pt}_2(\mu\text{-P}_2\text{O}_5\text{H}_2)_4]^{4-}$ structure shown in Figure 1, similarities and differences were found between the calculated and experimental parameters (Table 1). The bond angles and the P–O₁ bond lengths were in excellent agreement with the X-ray results, and, as expected from the X-ray results, the Pt atoms were about 0.02 \AA below the approximate plane defined by the four P atoms adjacent to Pt. However, the Pt–P bonds were longer than the experimental values. The two Pt-tetra-phosphite units were 0.11 \AA further apart in the optimized geometry relative to the X-ray structure. These results obtained with one of the largest basis sets appear satisfactory despite the shortcomings associated with the calculation of the metal–ligand bond lengths using B3LYP theory.^{7,15}

In the LLTS, most geometry parameters did not change significantly as compared to the singlet ground state. However,

TABLE 3: Calculated Singlet and Triplet Excited States in the Gas Phase and in Water Based on the SGS Geometry^a

state	$E_{\text{VER}}, \times 10^3 \text{ cm}^{-1}$	f	$\psi_o \rightarrow \psi_v$	type	$E_{\text{EXP}}, \times 10^3 \text{ cm}^{-1}$
Singlet Excited States in the Gas Phase					
2	27.24	0.215	164 \rightarrow 166 (0.7)	Pt _{s,dxy,dx2-y2,dz2} \rightarrow Pt _s	27.20
5	30.08	0.018	161 \rightarrow 165 (0.7)	O, P, Pt _{pz} , P \rightarrow Pt _{s,py}	
6	30.09	0.018	160 \rightarrow 165 (0.7)	O, P, Pt _{px} \rightarrow Pt _{s,py}	
7	32.45	0.010	163 \rightarrow 166 (0.7)	O, P, Pt _{pz} \rightarrow Pt _s	33.00
8	32.46	0.010	162 \rightarrow 166 (0.7)	O, P, Pt _{px} \rightarrow Pt _s	33.00
13	33.82	0.067	164 \rightarrow 167 (0.7)	Pt _{s,dxy,dx2-y2,dz2} \rightarrow Pt _s	
Triplet Excited State in the Gas Phase					
1	22.73	0	164 \rightarrow 166 (0.7)	Pt _{s,dxy,dx2-y2,dz2} \rightarrow Pt _s	22.10
Singlet Excited States in Water					
1	27.80	0.384	164 \rightarrow 165 (0.7)	Pt _{s,dxy,dx2-y2,dz2} \rightarrow Pt _{py,s} , O	27.20
4	36.16	0.015	163 \rightarrow 165 (0.6)	O, P, Pt _{pz} \rightarrow Pt _{py,s} , O	37.00
5	36.17	0.016	162 \rightarrow 165 (0.6)	O, P, Pt _{px} \rightarrow Pt _{py,s} , O	37.00
Triplet Excited State in Water					
1	22.81	0	164 \rightarrow 165 (0.7)	Pt _{s,dxy,dx2-y2,dz2} \rightarrow Pt _{py,s} , O	22.10

^a E_{VER} is the energy of the vertical transition, f is the oscillator strength, and ψ_o and ψ_v are the occupied and the virtual orbitals that define the transition. The transition type is determined on the basis of the change in the spatial distribution from the occupied to the virtual orbital. The transition coefficient for each transition is given in parentheses. E_{EXP} is the experimental energy from ref 4d. (See text for calculation details.)

there was a dramatic change in the distance between the two Pt-tetraphosphite units. The metal–metal distance was reduced by 0.22 Å, which represents a 7% Pt–Pt bond shrinkage in LLTS relative to SGS. The same methodology produced a 4% shrinkage for [Pt(bph)(CO)₂] in the LLTS relative to the SGS.^{3c} On the other hand, the P₁–P_{1'} distance shortened by only 1.6%, leaving the metal atom 0.05 Å below the plane of the four adjacent P atoms. The Pt–P bond was longer by 0.02 Å in the LLTS relative to the SGS as reported previously.^{6c} This elongation is reasonable considering the molecular orbital distribution changes.

The change in the Pt–Pt distance in the triplet state of [Pt₂(μ-P₂O₅H₂)₄]^{4−} has been investigated experimentally in detail. High-quality triplet absorption and phosphorescence emission spectra of Ba₂[Pt₂(μ-P₂O₅H₂)₄] in the solid state at 10 K were used for evaluation of the metal–metal interaction of the complex in singlet and triplet states. On the basis of Lorentzian fits to the spectral progressions¹⁶ for the two spectra and assignment of the Pt–Pt stretch taken from the Raman spectrum, it was concluded that the Pt–Pt bond was shorter by 0.21 Å in the triplet state as compared to the singlet state.^{4c} This represents 7% relative bond shortening – the same as found through B3LYP. Other experimental reports give values of 6% and 9% for the Pt–Pt bond shortening.⁶ Our result is comparable to the result reported by Coppens et al. using the zero-order regular approximation (ZORA) and the PW86LYP functional.^{6c}

Orbital Population Analysis. The percent molecular orbital populations of selected SGS orbitals of [Pt₂(μ-P₂O₅H₂)₄]^{4−} in the gas phase and in aqueous solution are listed in Table 2. The orbital energy diagram is shown in Figure 3. The purpose of the orbital analysis is to make bond assignments with respect to the Pt atom in [Pt₂(μ-P₂O₅H₂)₄]^{4−} and account for optical transitions found experimentally. In the gas phase (Table 2A), there are pairs of degenerate orbitals at 35 220 and 35 680 cm^{−1} that were located on the nonbridging oxygen and the phosphorus atoms. The orbitals of the first pair (160 and 161) associated with 35 220 cm^{−1} featured a 27.4% metal p_x contribution and a 32.3% metal p_z contribution for 160 and 161, respectively. The other pair (162 and 163) associated with 35 680 cm^{−1} were located mainly on the pyrophosphite bridges with only about a 20% metal p_x contribution and a 24% metal p_z contribution for 162 and 163, respectively. The predominantly metal-centered orbital 164 (HOMO) was 6000 cm^{−1} higher in energy. It featured 18.3% metal d_{x2-y2} and 20.2% metal d_{xy} character and

was assigned as a metal–metal antibonding orbital. The orbital 165 (LUMO) was 27 190 cm^{−1} higher in energy than the HOMO and had 79% metal s and 16% metal p_y orbital contributions. The LUMO was antibonding with respect to the Pt–Pt bond. The virtual orbitals 166 and 167 were Pt–Pt bonding (Figure 2C) and had metal s contributions that were higher than 87%.

The molecular orbitals were calculated for the complex in aqueous solution using the CPCM method based on the gas-phase geometry. The orbital energies and populations of molecular orbitals 160–167 changed dramatically in aqueous solution (Table 2B and Figure 3) as compared to in the gas phase. The metal p_x population of orbital 160 decreased from 27.4% in the gas phase to 19.2% in water, and the electron density partially shifted to the p_z orbital of Pt where its contribution in water reached 6.3% as compared to only 0.2% in the gas phase. For orbital 161, the metal p_z population dropped from 32.3% in the gas phase to 22.6% in water. The percent contribution of the orbitals located on the pyrophosphite bridge atoms, on the other hand, increased to 28.9% for P and 39.3% for O in aqueous solution as compared to 26.8% for P and 36.9% for O in the gas phase. The percent contributions and the bonding character of the molecular orbitals 162 and 163 (Figure 2A) did not change significantly in aqueous solution relative to the gas phase. In water, orbital 164 (HOMO) featured 41.4% metal d_{xy} and d_{x2-y2} and 26.5% metal s orbital contributions (Figure 2B). Orbital 165 (LUMO) containing 32% metal p_y character was located 33 760 cm^{−1} above the HOMO. The metal s share in the LUMO in aqueous solution had dropped from 79.0% to 26.1% in the gas phase. With 26% metal s contributions, the LUMO was classified as metal p_y centered and Pt–Pt bonding (Figure 2B). The virtual orbitals 166 and 167 were mainly located on the P atoms of the pyrophosphite bridges with populations of 55.7% and 66.6%, respectively. Both had metal d_{z2} contributions of 15.5% each. There were no metal s contributions of these orbitals in water. Our determinations for the orbital contributions of the HOMO and the LUMO in water were in very good agreement with the assignment by Fordyce et al.^{4d} where the HOMO contained d orbitals and the LUMO contained metal p orbitals along the Pt–Pt bond.

The energies of the occupied molecular orbitals (117–164) in the gas phase were positive, but in water they were negative (Figure 3). The energy of the HOMO (orbital 164), for example, decreased from 41 620 cm^{−1} in the gas phase to −44 860 cm^{−1}

in water. In addition, the energies of the four virtual orbitals 165–168 in water were negative. Consequently, the solvent effect result, in this case water, lowered orbital energies from positive to negative stabilizing $[\text{Pt}_2(\mu\text{-P}_2\text{O}_5\text{H}_2)_4]^{4-}$.

HOMO to LUMO Transition. The lowest-energy electronic transition for $[\text{Pt}_2(\mu\text{-P}_2\text{O}_5\text{H}_2)_4]^{4-}$ is the HOMO to LUMO transition which occurs to the first singlet excited state. In the gas phase, the HOMO is located on the metal *s* and metal d_{xy} and $d_{x^2-y^2}$ orbitals. The LUMO is located on the metal *s* orbital with a small metal p_y contribution. The HOMO and the LUMO are antibonding with respect to the Pt–Pt bond.

In aqueous solution, the spatial distribution of the HOMO is similar to that in the gas phase, but the LUMO is mainly located on the metal p_y orbital. The most important change, however, is that the LUMO in water is bonding. The lowest-energy transition in water is metal $s^* \rightarrow$ metal p_y . This generates two metal p_y orbitals of the same phase, one on Pt_1 and the other on Pt_2 . A predominantly metal *p*–*p* σ -bond is created between the two platinum atoms upon excitation of a single electron from the antibonding HOMO to the bonding LUMO in water (Figure 2B). This bond formation accounts for the 7% Pt–Pt bond shortening as noted above in the LLTS relative to the SGS. Our result, while containing some metal *s* character, is in general agreement with the metal $d^* \rightarrow$ metal *p* assignment reported from measurements using a single crystal of $\text{K}_4[\text{Pt}_2(\mu\text{-P}_2\text{O}_5\text{H}_2)_4]$.^{4c}

Singlet Excited States. Six singlet excited states based on the SGS geometry in the gas phase are listed in Table 3 along with the experimental absorption energies.^{4d} The energy of singlet excited state 1 was calculated to be 23 760 cm^{-1} , but the oscillator strength was zero. Singlet excited state 2 at 27 240 cm^{-1} , based on an electronic transition of primarily metal d^* and $s^* \rightarrow$ metal *s* (orbital 164 \rightarrow orbital 166, Figure 2C), featured the highest oscillator strength of 0.215. This state is associated with the formation of a metal *s*–*s* σ bond between the platinum atoms in the gas phase. Because excited state 1 has zero oscillator strength whereas the oscillator strength of excited state 2 is large, the observed transition in the gas phase will be from the HOMO to LUMO+1.

The higher energy excited states are related to the following analysis. As shown in Table 3, excited states 5–8 were ligand-to-metal charge transfer (LMCT) states and involved transitions between occupied orbitals 160–163 located on the pyrophosphate bridge and the metal *s* centered orbitals 165 and 166. Excited states 5 and 6 were degenerate. They were due to transitions from orbitals 160 and 161 located both on the P–O–P bridge and on metal *p* to orbital 165. Similarly, excited states 7 and 8 were based on electronic transitions from the 162 and 163 pair of degenerate P–O–P orbitals to the metal *s* centered orbital 166. Excited state 13 had high oscillator strength and was similar in type to excited state 2 (metal d^* and $s^* \rightarrow$ metal *s*).

Similar to the SGS molecular orbital assignments, the energies and the types of the singlet excited states showed variations in aqueous solution as compared to the gas phase. For excited state 1 in water, the HOMO to LUMO transition (Figure 2B) occurs between the metal *d* orbitals and the metal *p* orbitals, where both are located along the metal–metal bond in agreement with results reported previously from experiment.^{4c} Excited states 4 (Figure 2A) and 5 located at 36 160 cm^{-1} were degenerate LMCT states and differed from the excited states in the gas phase. Instead of metal *s* parentage, they now were metal *p_y* based.

The calculated energy of singlet excited state 2 in the gas phase was only 40 cm^{-1} higher than that of the most intense experimentally determined absorption peak in water. Excited states 7 and 8 in the gas phase were $\sim 550 \text{ cm}^{-1}$ lower in energy than the experimental value of 33 000 cm^{-1} . In water, excited state 1 was higher in energy relative to the experimental absorption energy by 600 cm^{-1} . Excited states 4 and 5 were 800 cm^{-1} lower in energy as compared to the 37 000 cm^{-1} peak observed experimentally in aqueous solution. Overall, the excited-state energies correlated very well with the experimental values. These energies were calculated using the SGS geometry optimized in the gas phase and despite the differences noted above are considered reliable.

The molar absorptivity coefficients were determined using eq 1 both in the gas and in the liquid phase, but the comparisons below are to the experimental results in water. The ϵ value of 29 000 $\text{M}^{-1} \text{ cm}^{-1}$ calculated for excited state 2 in the gas phase was in a good agreement with the experimental value of 33 500 $\text{M}^{-1} \text{ cm}^{-1}$ for the most intense absorption peak in aqueous solution.^{4d} Excited states 7 and 8 have calculated molar absorptivities of 1360 $\text{M}^{-1} \text{ cm}^{-1}$ each, as compared to 850 $\text{M}^{-1} \text{ cm}^{-1}$ found experimentally in water. The calculated ϵ for the metal-centered excited state 1 in water was 52 000 $\text{M}^{-1} \text{ cm}^{-1}$, about 1.5 times higher than the experimental value of 33 500 $\text{M}^{-1} \text{ cm}^{-1}$ in the same solvent. The calculated LMCT excited states 4 and 5 in water produced ϵ values of 2000 and 2200 $\text{M}^{-1} \text{ cm}^{-1}$, respectively. They sum together to give an ϵ value of 4200 $\text{M}^{-1} \text{ cm}^{-1}$ at about 36 165 cm^{-1} . This value was higher than the experimental ϵ of 1360 $\text{M}^{-1} \text{ cm}^{-1}$ for the peak at 37 000 cm^{-1} .^{4d} The calculated molar absorptivity in the gas phase at 27 240 cm^{-1} was in reasonable agreement with the experimental values, but those in water were higher as noted previously.^{7a,b}

Triplet Excited States. The complex $[\text{Pt}_2(\mu\text{-P}_2\text{O}_5\text{H}_2)_4]^{4-}$ has been extensively studied for its phosphorescence excitation and emission properties. An absorption peak associated with phosphorescence excitation at 22 100 cm^{-1} ($\epsilon = 100 \text{ M}^{-1} \text{ cm}^{-1}$)^{4d} was reported and assigned as a forbidden singlet to triplet transition. Intense phosphorescence at 19 400 cm^{-1} from the populated triplet state to the singlet ground state was observed in aqueous solution as well as in the solid state.⁴

The phosphorescence excitation was expected to occur from the SGS geometry following the Franck–Condon principle. The calculated energy of the multiplicity-forbidden triplet excited state 1 in the gas phase¹⁷ was 22 730 cm^{-1} . It was based on a metal *s* and *d* (antibonding) \rightarrow metal *s* (bonding) transition (Figure 2C). The calculated energy was 630 cm^{-1} higher than the experimental value. This triplet excited state would account for the reduction of the Pt–Pt bond distance in the gas phase.

Triplet excited state 1 in water was based on the antibonding HOMO (metal *d* and *s*) \rightarrow bonding LUMO (metal p_y) transition. It was 710 cm^{-1} higher in energy relative to the experimental value.^{4d} This triplet excited state accounts for the reduction of the Pt–Pt bond distance in water. The TDDFT formalism does not include a spin–orbit coupling treatment which for third row transition metals could lower the predicted triplet state energy through interactions with higher singlet and triplet excited states.^{3a} Triplet excited states 1 in water and in the gas phase involve transitions from the Pt–Pt antibonding HOMO to a Pt–Pt bonding molecular orbital (Figure 2B and C). This transition caused the geometry changes in the triplet state.

Upon absorption of light at the phosphorescence excitation energy and population of the Pt–Pt bonding orbital, the geometry of the ion would be altered to accommodate the new electronic environment. To investigate the phosphorescence

emission state of $[\text{Pt}_2(\mu\text{-P}_2\text{O}_5\text{H}_2)_4]^{4-}$, the geometry of the LLTS was optimized in the gas phase. This state is produced by the stabilization of the triplet excited state 1 and the population of Pt–Pt bonding orbital 166 in the gas phase. The $E_{(\text{UB}+\text{HF-LYP})}$ of the LLTS was higher than that of the SGS by 21 980 cm^{-1} in the gas phase (UB = unrestricted Becke, HF = Hartree–Fock, LYP = Lee, Yang, and Parr).⁸ The energy difference between the geometry of LLTS calculated at singlet multiplicity and the SGS was $\sim 1500 \text{ cm}^{-1}$. The remainder, 20 480 cm^{-1} , was due to the spin-forbidden singlet to triplet transition HOMO \rightarrow 166 (Figure 2C). The latter value is 1080 cm^{-1} higher than the experimental phosphorescence emission energy of 19 400 cm^{-1} . This is similar to results reported for analogous systems.³

Conclusion

DFT calculations revealed that the complex ion $[\text{Pt}_2(\mu\text{-P}_2\text{O}_5\text{H}_2)_4]^{4-}$ underwent 7% shrinkage in the metal–metal distance in the LLTS as compared to SGS. This bond shortening was in excellent agreement with experimental high-resolution spectral studies but was larger than the calculated value for the dimers of $[\text{Pt}(\text{bph})(\text{CO})_2]$. Upon single electron occupancy of the HOMO and orbital 166, formation of a predominantly metal s–s σ -bond in the gas phase occurred. In water, a predominantly metal p–p σ -bond is created upon the HOMO \rightarrow LUMO transition. Analysis of the singlet excited states in the gas phase and in aqueous solution revealed fundamental changes in the frontier orbital populations and energies upon addition of solvent effects. The lowest-lying triplet excited-state energy, determined on the basis of the SGS geometry, was correlated with the phosphorescence excitation energy. The LLTS geometry was optimized, and its energy was found to be 1080 cm^{-1} higher than the phosphorescence emission energy.

Acknowledgment. We acknowledge the support of Kansas NSF Cooperative Agreement EPS 987432, the Wichita State University High Performance Computing Center, the Wichita State University Office of Research Administration, the Department of Energy, and Parker Fellowships (S.R.S. and J.M.V.). We also thank Dr. David M. Eichhorn for helping us to access the Inorganic Crystal Structure Database.

Supporting Information Available: The optimized geometries of $[\text{Pt}_2(\mu\text{-P}_2\text{O}_5\text{H}_2)_4]^{4-}$ in the SGS and in LLTS as well as in the singlet and triplet excited states in the gas phase and in water. This material is available free of charge via the Internet at <http://pubs.acs.org>.

References and Notes

- (1) (a) Connick, W. B.; Marsh, R. E.; Schaefer, W. P.; Gray, H. B. *Inorg. Chem.* **1997**, *36*, 912–922. (b) Ratilla, E. M. A.; Scott, B. K.; Moxness, M. S.; Kostic, N. M. *Inorg. Chem.* **1990**, *29*, 918–926. (c) Miskowski, V. M.; Houlding, V. H. *Inorg. Chem.* **1991**, *30*, 4446–4452. (d) Gliemann, G.; Yersin, H. *Struct. Bonding* **1985**, *62*, 87–161.
- (2) (a) Zheng, G. Y.; Rillema, D. P. *Inorg. Chem.* **1998**, *37*, 1392–1397. (b) Fleeman, W. L.; Connick, W. B. *The Spectrum* **2002**, *15*, 14–19. (c) Chan, C. W.; Lai, T. F.; Che, C. M.; Peng, S. M. *J. Am. Chem. Soc.* **1993**, *115*, 11245–11253.
- (3) (a) Makedonas, C.; Mitsopoulou, C. A.; Lahoz, F. J.; Balana, A. I. *Inorg. Chem.* **2003**, *42*, 8853–8865. (b) Benito, J.; Berenguer, J. R.; Fornies, J.; Gil, B.; Gomez, J.; Lalinde, E. *Dalton Trans.* **2003**, *22*, 4331–4339. (c) Stoyanov, S. R.; Villegas, J. M.; Rillema, D. P. *Inorg. Chem.* **2003**, *42*, 7852–7860.
- (4) (a) Roundhill, D. M.; Sperline, R. P.; Beaulieu, W. B. *J. Chem. Soc., Chem. Comm.* **1977**, *1*, 62–63. (b) Che, C.-M.; Butler, L. G.; Gray, H. B. *J. Am. Chem. Soc.* **1981**, *103*, 7769–7797. (c) Rice, S. F.; Gray, H. B. *J. Am. Chem. Soc.* **1983**, *105*, 4571–4575. (d) Fordyce, W. A.; Brummer, J. G.; Crosby, G. A. *J. Am. Chem. Soc.* **1981**, *103*, 7061–7064. (e) Zipp, A. P. *Coord. Chem. Rev.* **1988**, *84*, 47–83.
- (5) (a) Filomena Dos Remedios Pinto, M. A.; Sadler, P. J.; Neidle, S.; Sanderson, M. R.; Subbiah, A.; Kuroda, R. J. *J. Chem. Soc., Chem. Commun.* **1980**, 13–15. (b) Marsh, R. E.; Herstein, F. H. *Acta Crystallogr., Sect. B* **1983**, *39*, 280–287.
- (6) (a) Kim, C. D.; Pillet, S.; Wu, G.; Fullagar, W. K.; Coppens, P. *Acta Crystallogr., Sect. A* **2002**, *A58*, 133–137. (b) Coppens, P.; Novozhilova, I. V. *Faraday Discuss.* **2002**, *122*, 1–11. (c) Novozhilova, I. V.; Volkov, A. V.; Coppens, P. *J. Am. Chem. Soc.* **2003**, *125*, 1079–1087. (d) Gellene, G. I.; Roundhill, D. M. *J. Phys. Chem. A* **2002**, *106*, 7617–7620.
- (7) (a) Stoyanov, S. R.; Villegas, J. M.; Rillema, D. P. *Inorg. Chem. Commun.* **2004**, *7*, 838–841. (b) Villegas, J. M.; Stoyanov, S. R.; Huang, W.; Lockyear, L. L.; Reibenspies, J.; Rillema, D. P. *Inorg. Chem.* **2004**, submitted. (c) Barone, V.; Fabrizi de Biani, F.; Riuz, E.; Sieklucka, B. *J. Am. Chem. Soc.* **2001**, *123*, 10742–10743.
- (8) (a) Becke, A. D. *J. Chem. Phys.* **1993**, *98*, 5648–5652. (b) Lee, C.; Yang, W.; Parr, R. G. *Phys. Rev. B* **1988**, *37*, 785–789. (c) Vosko, S. H.; Wilk, L.; Nusair, M. *Can. J. Phys.* **1980**, *58*, 1200–1211.
- (9) Frisch, M. J.; Trucks, G. W.; Schlegel, H. B.; Scuseria, G. E.; Robb, M. A.; Cheeseman, J. R.; Montgomery, J. A., Jr.; Vreven, T.; Kudin, K. N.; Burant, J. C.; Millam, J. M.; Iyengar, S. S.; Tomasi, J.; Barone, V.; Mennucci, B.; Cossi, M.; Scalmani, G.; Rega, N.; Peterson, G. A.; Nakatsuji, H.; Hada, M.; Ehara, M.; Toyota, K.; Fukuda, R.; Hasegawa, J.; Ishida, M.; Nakajima, T.; Honda, Y.; Kitao, O.; Nakai, H.; Klene, M.; Li, X.; Knox, J. E.; Hratchian, H. P.; Cross, J. B.; Adamo, C.; Jaramillo, J.; Gomperts, R.; Stratmann, R. E.; Yazyev, O.; Austin, A. J.; Cammi, R.; Pomelli, C.; Ochterski, J. W.; Ayala, P. Y.; Morokuma, K.; Voth, G. A.; Salvador, P.; Dannenberg, J. J.; Zakrzewski, V. G.; Dapprich, S.; Daniels, A. D.; Strain, M. C.; Farkas, O.; Malick, D. K.; Rabuck, A. D.; Raghavachari, K.; Foresman, J. B.; Ortiz, J. V.; Cui, Q.; Baboul, A. G.; Clifford, S.; Cioslowski, J.; Stefanov, B. B.; Liu, G.; Liashenko, A.; Piskorz, P.; Komaromi, I.; Martin, R. L.; Fox, D. J.; Keith, T.; Al-Laham, M. A.; Peng, C. Y.; Nanayakkara, A.; Challacombe, M.; Gill, P. M. W.; Johnson, B.; Chen, W.; Wong, M. W.; Gonzalez, C.; Pople, J. A. *Gaussian 03*, revision B.03; Gaussian, Inc.: Pittsburgh, PA, 2003.
- (10) (a) Andrae, D.; Hauessermann, U.; Dolg, M.; Stoll, H.; Preuss, H. *Theor. Chim. Acta* **1990**, *77*, 123–141. (b) Dunning, T. H., Jr.; Hay, P. J. In *Modern Theoretical Chemistry*; Schaefer, H. F., III, Ed.; Plenum: New York, 1976; Vol. 3, pp 1–28. (c) McLean, A. D.; Chandler, G. S. *J. Chem. Phys.* **1980**, *72*, 5639. (d) Krishnan, R.; Binkley, J. S.; Seeger, R.; Pople, J. A. *J. Chem. Phys.* **1980**, *72*, 650.
- (11) (a) Stratmann, R. E.; Scuseria, G. E.; Frisch, M. J. *J. Chem. Phys.* **1998**, *109*, 8218–8224. (b) Bauernschmitt, R.; Ahlrichs, R. *Chem. Phys. Lett.* **1996**, *256*, 454. (c) Casida, M. E.; Jamorski, C.; Casida, K. C.; Salahub, D. R. *J. Chem. Phys.* **1998**, *108*, 4439.
- (12) (a) Barone, V.; Cossi, M. *J. Phys. Chem. A* **1998**, *102*, 1995. (b) Cossi, M.; Rega, N.; Scalmani, G.; Barone, V. *J. Comput. Chem.* **2003**, *24*, 669–681. (c) Cossi, M.; Barone, V. *J. Phys. Chem. A* **2001**, *105*, 4708–4717.
- (13) Geometry optimization in aqueous solution was not achieved. The geometry produced through partial optimization did not represent as good of a starting geometry for the TDDFT calculations as did the gas-phase optimized geometry.
- (14) Foresman, J. B.; Frisch, A. E. *Exploring Chemistry with Electronic Structure Methods*, 2nd ed.; Gaussian, Inc.: Pittsburgh, PA, 1996; Vols. 259–260, p 215.
- (15) (a) Monat, J. E.; Rodriguez, J. H.; McCusker, J. K. *J. Phys. Chem. A* **2002**, *106*, 7399–7406. (b) Rodriguez, J. H.; Wheeler, D. E.; McCusker, J. K. *J. Am. Chem. Soc.* **1998**, *120*, 12051–12068.
- (16) (a) Ballhausen, C. J. *Molecular Electronic Structures of Transition Metal Complexes*; McGraw-Hill: London, 1979; pp 132–135. (b) Rice, S. F. Ph.D. Thesis, California Institute of Technology, 1982.
- (17) The oscillator strength of the multiplicity forbidden state would be zero. Gaussian 03 has a minimum limit of 1×10^{-4} for f , and a more precise value cannot be determined.